



ELSEVIER

Contents lists available at ScienceDirect

Journal of Sound and Vibration

journal homepage: www.elsevier.com/locate/jsv

Simultaneous energy harvesting and vibration control in a nonlinear metastructure: A spectro-spatial analysis

Mohammad Bukhari, Oumar Barry*

Department of Mechanical Engineering, Virginia Tech, Blacksburg, VA, 24061, USA



ARTICLE INFO

Article history:

Received 2 August 2019
 Revised 14 November 2019
 Accepted 27 January 2020
 Available online 7 February 2020
 Handling Editor: E Pavlovskaja

Keywords:

Nonlinear metamaterial
 Energy harvesting
 Spectro-spatial analysis
 Acoustics diode
 Solitary waves

ABSTRACT

Considerable attention has recently been given to the study of simultaneous energy harvesting and vibration attenuation in metastructures. However, only linear metastructures were investigated although nonlinear metastructures and nonlinear electromechanical devices offer superior interesting wave propagation phenomena (e.g., birth of solitary waves, tunable bandgap, acoustic nonreciprocity) and broadband energy harvesting. In this paper, we investigate the wave propagation in a weakly nonlinear metastructure with electromechanical resonators. Explicit expressions are derived for the nonlinear dispersion relations using the method of multiple scales. These expressions are validated via direct numerical integration. We carried out parametric studies to investigate the role of different parameters of the electromechanical resonators on the linear and nonlinear band structure. To obtain further detailed information on the nonlinear wave propagation, we employ spectro-spatial analysis on the numerical simulations. This spectro-spatial analysis can reveal the output voltage distortion due to different types of nonlinearities. The results indicate that nonlinear chain can enhance energy harvesting through the birth of solitary wave and without degrading the boundary of the bandgap. The results also suggest that such a system is suitable for designing electromechanical diodes and rectifiers.

© 2020 Elsevier Ltd. All rights reserved.

1. Introduction

Metastructures are artificially engineered structures offering exceptional and unique properties that are not present in conventional homogeneous structures [1]. They were originally developed for optical wave propagation (also known as metamaterials) and then they were extended to enhance elastic and wave propagation properties [2]. Some of these properties are negative mass, negative density, and negative Poisson's ratio [3]. These unique features suggest that metastructures can be beneficial in vibration and noise control, non-destructive testing, energy harvesting, and acoustic rectifiers.

Metastructures are usually arranged in specific patterns that exhibit exotic functionalities. Earlier consideration of metastructures studied periodic structures [4–9]. Periodic structures prevent the wave from propagating through the structure at range of frequencies known as bandgap and caused by Bragg scattering. These frequencies have wavelengths close to the lattice constant. This bandgap formation can be employed in low-frequency vibration attenuation.

The limitation on the lattice size in Bragg scattering restricts the application of metamaterials to only large structures; however, many engineering applications require controlling smaller size components. Inspired by smaller size systems, Liu et al. [10] introduced local resonators in metastructures to control vibrations at wavelengths much smaller than the lattice constant.

* Corresponding author.

E-mail address: obarry@vt.edu (O. Barry).

These structures are called locally-resonant metamaterials and they are capable of widening the original bandgap developed by Bragg scattering. Indeed, the parameters of the local resonator determine the dominant cause of the bandgap [11]. Moreover, multiple bandgaps can be obtained by using multiple resonators with different parameters [12,13].

For large wave amplitudes in inherently nonlinear mediums, linear theory cannot adequately represent the problem; thus higher-order nonlinear terms need to be considered. Nonlinear metastructures exhibit some interesting wave propagation phenomena that do not develop in linear metastructures. Some of those are gap solitons [14], envelope and dark solitons [15], asymmetric wave propagation [16], and adjustable bandgap [17].

Nonlinear problems can be characterized based on the strength of nonlinearities. When the nonlinearity is weak, the problem can be handled by perturbation techniques [18,19] and approximate analytical solution can be derived when the problem asymptotically converges. Weakly nonlinear metastructures were investigated by Narisetti et al. [20]. They employed Lindstedt-Poincare method to derive explicit expressions for the dispersion relations. However, when several nonlinear waves propagate and interact through the structure, the method of multiple scales is more suitable since the associated algebra requires less efforts [21]. Strongly nonlinear metastructures have gained less attention in the literature and they usually require other techniques such as the complexification-averaging or shooting methods to tackle the problem [22].

Analyzing the dispersion relation analytically does not provide adequate information about the nonlinear dynamical features in metastructures. Instead, it only presents the nonlinear shift in the dispersion curves. To reveal other interesting features, Ganesh and Gonella [23] employed spectro-spatial analysis to investigate the wave propagation through metastructures. Their analysis provided more detailed information about the wave distribution in the structure (i.e., localized or dispersive waves); therefore, the birth and inhalation of solitary waves can be predicted based on the wavelength and nonlinearity type. The use of spectro-spatial analyses were also extended in Refs. [24,25] for locally resonant metastructures. They observed a significant frequency shift in the optical branch, and they then employed this shift to design acoustics diodes.

In recent years, many researchers investigated the bandgap formation due to electromechanical coupling in metastructures with piezoelectric patches [26–30]. The electromechanical coupling generates piezoelectric locally bandgap where the dimension of the bandgap is controlled by the added stiffness to the system. Embedding piezoelectric materials in metastructures can also lead to simultaneous energy harvesting and vibration attenuation [31]. This is inspired by the flat band of frequencies in metastructures, which was experimentally demonstrated using a locally resonant phononic crystal plate with embedded spiral beams [32]. The problem was theoretically investigated later for a discrete structure in Ref. [31] and for a continuous structure in Ref. [33]. Moreover, Hu et al. [34] extended the problem by coupling the internal resonators. This showed an improvement in the energy harvesting and vibration suppression. Energy harvesting in metastructures was also experimentally demonstrated by testing a 3D printed 2D structure in Ref. [35]. Furthermore, traveling wave energy harvesting was also experimentally and numerically demonstrated in a 2D phononic crystal lens structure. The authors showed that a significance improvement in energy harvesting can be achieved when the acoustic metamaterial is designed to focus or properly localize the wave energy [36,37].

The study of simultaneous energy harvesting and vibration attenuation in metastructures has so far been limited to linear metastructures. There is no study that investigates the effect of nonlinearity in metastructures for simultaneous energy harvesting and vibration control. In this paper, we investigate the wave propagation and energy harvesting in a weakly nonlinear metastructure with local electromechanical resonators. We employ the method of multiple scales to derive explicit expressions for the dispersion relations. These relations are validated by direct numerical integration. Then, we study various nonlinear phenomena and their effects on the energy harvesting distribution and magnitude. This is done through studying the relation between topological (i.e., space-time domain) and spectral (dispersion relations) features of a wave propagating in such a nonlinear metastructure. Parametric studies are conducted to investigate the effect of different parameters on the band structure, the role of nonlinearity on energy harvesting, and energy harvesting associated with solitary waves.

The rest of the paper is outlined as follows: In Section 2, we model the nonlinear chain and electromechanical resonators. We then present an approximate closed form solution for the dispersion relations. These relations are discussed and validated numerically in Section 3. In Section 4, we investigate the topological features of the output voltage wave by spectro-spatial analysis to demonstrate more detailed information about nonlinear wave propagation phenomena. Finally, we discuss the obtained results in Section 5, and then summarize our findings in Section 6.

2. Mathematical modeling

A schematic diagram for the proposed metastructure is shown in Fig. 1. The metastructure is presented by a chain of cells. Each cell consists of a rigid mass, M , and is connected to other cells by a nonlinear spring with linear coefficient, K , and nonlinear coefficient, $\bar{\alpha}$. The cell is also connected to a local electromechanical resonator with an effective mass, m_p , and an effective linear stiffness k_1 . The resonator consists of a substrate covered by a piezoelectric layer. This piezoelectric layer is shunted to an external resistor R_{eq} and it harvests a voltage, v . The displacement of the n th cell is defined as u_n , while the absolute displacement of its local resonator is Y_n . Following [31,38] the coupled equation of motions for each cell can be written as

$$M\ddot{u}_n + 2K\bar{u}_n - K\bar{u}_{n+1} - K\bar{u}_{n-1} + \bar{\alpha}(\bar{u}_n - \bar{u}_{n+1})^3 + \bar{\alpha}(\bar{u}_n - \bar{u}_{n-1})^3 + m_p(\ddot{u}_n + \ddot{Y}_n) = 0 \quad (1)$$

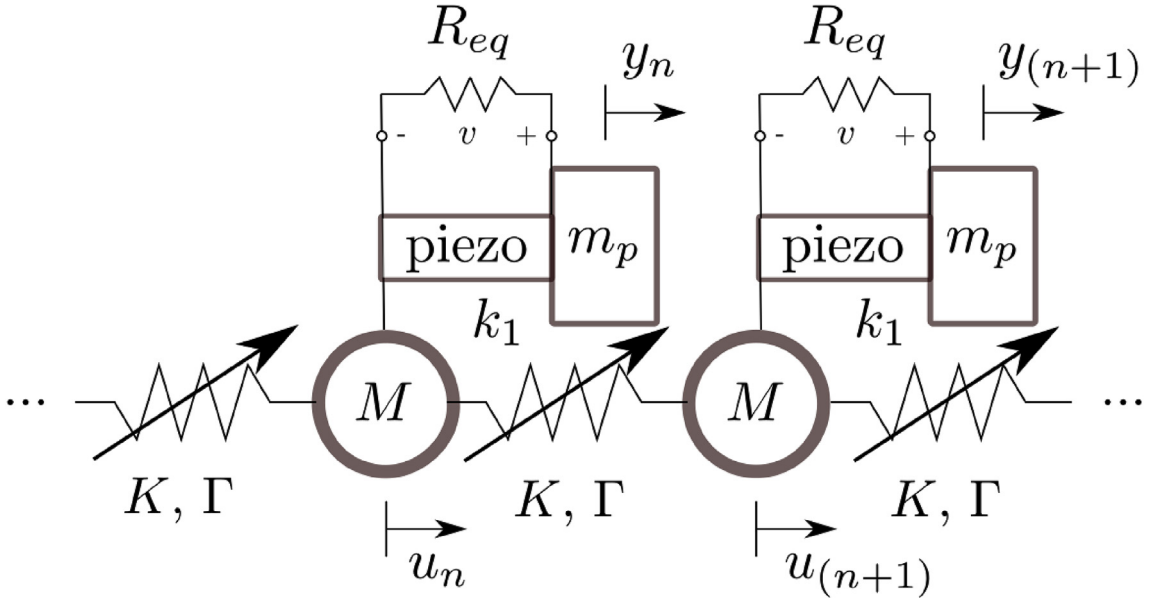


Fig. 1. A schematic diagram for the nonlinear acoustics metastructure with linear electromechanical resonator resonators.

$$m_p \ddot{u}_n + k_1 \bar{u}_n - \theta \bar{v}_n = -m_p \ddot{\bar{u}}_n \quad (2)$$

$$RC_p \dot{\bar{v}}_n + \bar{v}_n + R\theta \dot{\bar{u}}_n = 0 \quad (3)$$

where $\bar{u}_n = Y_n - \bar{u}_n$ is the relative displacement of the local resonator, θ is the electromechanical coupling coefficient, and C_p is the capacitance of the piezoelectric element. These equations can be written in normalized form as

$$\ddot{u}_n + 2u_n - u_{n+1} - u_{n-1} + \alpha(u_n - u_{n+1})^3 + \alpha(u_n - u_{n-1})^3 + \bar{k}\Omega_0^2(\dot{y}_n + \ddot{u}_n) = 0 \quad (4)$$

$$\Omega_0^2 \dot{y}_n + y_n - \alpha_1 v_n = -\Omega_0^2 \dot{u}_n \quad (5)$$

$$\alpha_2 \dot{v}_n + v_n + \alpha_3 \dot{y}_n = 0 \quad (6)$$

where $\omega_n^2 = K/M$, $\omega_d^2 = k_1/m_p$, $\bar{k} = k_1/K$, $u_n = \bar{u}_n/U_0$, $y_n = \bar{u}_n/y_0$, $v_n = \bar{v}_n/V_0$, $\alpha = \bar{\alpha}U_0^2/K$, $\Omega_0 = \omega_n/\omega_d$, $\alpha_1 = \theta V_0/k_1$, $\alpha_2 = RC_p \omega_n$, $\alpha_3 = R\theta \omega_n y_0/V_0$, and the nondimensional time is $\tau = \omega_n t$. We express the solution for the system by power series. By ignoring the terms of second order and higher, the solution can be written in the form

$$u_n(t, \epsilon) = u_{n0}(T_0, T_1) + \epsilon u_{n1}(T_0, T_1) + o(\epsilon^2) \quad (7)$$

$$y_n(t, \epsilon) = y_{n0}(T_0, T_1) + \epsilon y_{n1}(T_0, T_1) + o(\epsilon^2) \quad (8)$$

$$v_n(t, \epsilon) = v_{n0}(T_0, T_1) + \epsilon v_{n1}(T_0, T_1) + o(\epsilon^2) \quad (9)$$

where $T_0 = \tau$ is the fast time scale and $T_1 = \epsilon \tau$ is the slow time scale. Since the time is expressed in two independent variables, the time derivative can be presented using the chain rule as

$$(\dot{}) = D_0 + \epsilon D_1 + \dots \quad (10)$$

$$(\ddot{}) = D_0^2 + 2\epsilon D_0 D_1 + \dots \quad (11)$$

Introducing Eqs. (7)-(11) into Eqs. (4)-(6) and collecting the terms of similar coefficient leave us with the following sets of equations.

order ϵ^0

$$D_0^2 u_{n0} + 2u_{n0} - u_{(n-1)0} - u_{(n+1)0} + \bar{k}\Omega_0^2 D_0^2 (y_{n0} + u_{n0}) = 0 \quad (12)$$

$$\Omega_0^2 D_0^2 y_{n0} + y_{n0} - \alpha_1 v_{n0} = -\Omega_0^2 D_0^2 u_{n0} \quad (13)$$

$$\alpha_2 D_0 v_{n0} + v_{n0} + \alpha_3 D_0 y_{n0} = 0 \quad (14)$$

order ϵ^1

$$D_0^2 u_{n1} + 2u_{n1} - u_{(n-1)1} - u_{(n+1)1} + \bar{k}\Omega_0^2 D_0^2 (y_{n1} + u_{n1}) = -2\bar{k}\Omega_0^2 D_0 D_1 (y_{n0} + u_{n0}) - 2D_0 D_1 u_{n0} - \alpha v (u_{n0} - u_{(n-1)0})^3 - \alpha (u_{n0} - u_{(n+1)0})^3 \quad (15)$$

$$\Omega_0^2 D_0^2 y_{n1} + y_{n1} - \alpha_1 v_{n1} = -\Omega_0^2 D_0^2 u_{n1} - 2\Omega_0^2 D_0 D_1 u_{n0} - 2\Omega_0^2 D_0 D_1 y_{n0} \quad (16)$$

$$\alpha_2 D_0 v_{n1} + v_{n1} + \alpha_3 D_0 y_{n1} = -\alpha_2 D_1 v_{n0} - \alpha_3 D_1 y_{n0} \quad (17)$$

2.1. Linear dispersion relations

At order ϵ^0 , the problem is linear. The solution can be written as

$$u_n = A e^{i(nk - \omega\tau)} \quad (18)$$

$$y_n = B e^{i(nk - \omega\tau)} \quad (19)$$

$$v_n = C e^{i(nk - \omega\tau)} \quad (20)$$

Substituting Eqs. (19)-(20) into Eq. (14) yields

$$-i\alpha_2 \omega C + C - i\alpha_3 \omega B = 0 \quad (21)$$

Solving for C leaves us with

$$C = \Gamma B \quad (22)$$

where Γ is complex and can be written as

$$\Gamma = \frac{i\alpha_3 \omega}{1 - i\alpha_2 \omega} \quad (23)$$

Substituting Eqs. (18)-(19) and Eq. (22) into Eq. (13) leads to

$$B = K_\omega A \quad (24)$$

where K_ω is also complex and defined as follow

$$K_\omega = \frac{\Omega_0^2 \omega^2}{1 - \alpha_1 \Gamma - \Omega_0^2 \omega^2} \quad (25)$$

Finally, one can obtain the linear dispersion relation from Eqs. (12), (22) and (24) as:

$$-\omega^2 + (2 - 2 \cos k) - \bar{k}\Omega_0^2 \omega^2 (1 + K_\omega) = 0 \quad (26)$$

It is noteworthy here that Eq. (26) has five roots. Four of them are complex pairs with nonzero real part, while the fifth one is pure complex.

2.2. Nonlinear dispersion relation

At order ϵ the problem is nonlinear. We need to obtain the solvability condition in order to obtain a convergent approximate solution.

Equation. (17) can be written as (after multiplying by α_1)

$$(\alpha_2 D_0 + 1)\alpha_1 v_{n1} = \alpha_1 [-\alpha_3 D_0 y_{n1} - \alpha_2 D_1 v_{n0} - \alpha_3 D_1 y_{n0}] \quad (27)$$

Multiplying Eq. (16) by $(\alpha_2 D_0 + 1)$ and using Eq. (27) to eliminate v_{n1} , one can obtain

$$(\alpha_2 D_0 + 1)(\Omega_0^2 D_0^2 y_{n1} + y_{n1} + \Omega_0^2 D_0^2 u_{n1}) + \alpha_1 \alpha_3 D_0 y_{n1} = (\alpha_2 D_0 + 1)(-2\Omega_0^2 D_0 D_1 u_{n0} - 2\Omega_0^2 D_0 D_1 y_{n0}) - \alpha_2 \alpha_1 D_1 v_{n0} - \alpha_1 \alpha_3 D_1 y_{n0} \quad (28)$$

Equation (28) can be written as

$$[(\alpha_2 D_0 + 1)(\Omega_0^2 D_0^2 + 1) + \alpha_1 \alpha_3 D_0] y_{n1} = -(\alpha_2 D_0 + 1) \Omega_0^2 D_0^2 u_{n1} + (\alpha_2 D_0 + 1) (-2\Omega_0^2 D_0 D_1 u_{n0} - 2\Omega_0^2 D_0 D_1 y_{n0}) - \alpha_2 \alpha_1 D_1 v_{n0} - \alpha_1 \alpha_3 D_1 y_{n0} \tag{29}$$

Multiplying Eq. (29) by $\bar{k}\Omega_0^2 D_0^2$ and substituting it in Eq. (15) yields

$$[(\Omega_0^2 D_0^2 + 1)(\alpha_2 D_0 + 1) + \alpha_1 \alpha_3 D_0] ((1 + \bar{k}\Omega_0^2) D_0^2 u_{n1} + 2u_{n1} - u_{(n-1)1} - u_{(n+1)1}) - \bar{k}\Omega_0^2 D_0^2 (\alpha_2 D_0 + 1) \Omega_0^2 D_0^2 u_{n1} = [(\Omega_0^2 D_0^2 + 1)(\alpha_2 D_0 + 1) + \alpha_1 \alpha_2 D_0] (-2D_0 D_1 u_{n0} - 2\bar{k}D_0 D_1 (u_{n0} + y_{n0}) - \alpha(u_{n0} - u_{(n-1)0})^3 - \alpha(u_{n0} - u_{(n+1)0})^3 + \bar{k}\Omega_0^2 D_0^2 [-(\alpha_2 D_0 + 1) (-2\Omega_0^2 D_0 D_1 u_{n0} - 2\Omega_0^2 D_0 D_1 y_{n0})] + \alpha_1 \alpha_2 D_1 v_{n0} + \alpha_1 \alpha_3 D_1 y_{n0}] \tag{30}$$

To determine the solvability condition, one should substitute Eqs. (18)-(20) into Eq. (30) to obtain

$$[(\Omega_0^2 D_0^2 + 1)(\alpha_2 D_0 + 1) + \alpha_1 \alpha_3 D_0] ((1 + \bar{k}\Omega_0^2) D_0^2 u_{n1} + 2u_{n1} - u_{(n-1)1} - u_{(n+1)1}) - \bar{k}\Omega_0^2 D_0^2 (\alpha_2 D_0 + 1) \Omega_0^2 D_0^2 u_{n1} = [(-\Omega_0^2 \omega^2 + 1)(-i\alpha_2 \omega + 1) - i\alpha_1 \alpha_2 \omega] (2i\omega A' + 2i\omega \bar{k}\Omega_0^2 (1 + K_\omega) A' - 12\alpha A^2 \bar{A} (1 - \cos k)^2) - \bar{k}\Omega_0^2 \omega^2 [(i\omega \alpha_2 - 1)(2i\Omega_0^2 \omega A' + 2i\Omega_0^2 \omega K_\omega A') + \alpha_1 \alpha_2 K_\omega \Gamma A' + \alpha_1 \alpha_3 K_\omega A'] e^{i(nk - \omega t)} + NST \tag{31}$$

where NST denotes the non-secular terms.

The solvability condition can then be obtained as

$$[(-\Omega_0^2 \omega^2 + 1)(-i\alpha_2 \omega + 1) - i\alpha_1 \alpha_2 \omega] (2i\omega A' + 2i\omega \bar{k}\Omega_0^2 (1 + K_\omega) A' - 12\alpha A^2 \bar{A} (1 - \cos k)^2) - \bar{k}\Omega_0^2 \omega^2 [(i\omega \alpha_2 - 1)(2i\Omega_0^2 \omega A' + 2i\Omega_0^2 \omega K_\omega A') + \alpha_1 \alpha_2 K_\omega \Gamma A' + \alpha_1 \alpha_3 K_\omega A'] = 0 \tag{32}$$

Substituting the polar form ($A = ae^{ib}$ where a and b are functions of the slow time scale, $K_\omega = \text{Re}[K_\omega] + i\text{Im}[K_\omega]$, and $\Gamma = \text{Re}[\Gamma] + i\text{Im}[\Gamma]$) in Eq. (32) yields

$$- \frac{1}{2} \alpha_1 \alpha_2 \omega^2 \Omega_0^2 \bar{k} (\text{Re}[\Gamma] + i\text{Im}[\Gamma]) (e^{ib} a' + iae^{ib} b') (\text{Re}[K_\omega] + i\text{Im}[K_\omega]) + \alpha_2 \omega^2 \Omega_0^2 \bar{k} (e^{ib} a' + iae^{ib} b') (\text{Re}[K_\omega] + i\text{Im}[K_\omega]) + \frac{1}{2} \alpha_1 \alpha_3 \omega^2 \Omega_0^2 \bar{k} (e^{ib} a' + iae^{ib} b') (\text{Re}[K_\omega] + i\text{Im}[K_\omega]) + i\omega \Omega_0^2 \bar{k} (e^{ib} a' + iae^{ib} b') (\text{Re}[K_\omega] + i\text{Im}[K_\omega]) + \alpha_2 \omega^2 \Omega_0^2 \bar{k} (e^{ib} a' + iae^{ib} b') + \alpha_1 \alpha_3 \omega^2 \Omega_0^2 \bar{k} (e^{ib} a' + iae^{ib} b') + i\omega \Omega_0^2 \bar{k} (e^{ib} a' + iae^{ib} b') - \frac{3}{2} ia^3 \alpha \alpha_2 e^{ib} ccc \omega^3 \Omega_0^2 + \frac{3}{2} a^3 \alpha e^{ib} ccc \omega^2 \Omega_0^2 + \frac{3}{2} ia^3 \alpha \alpha_2 e^{ib} ccc \omega + \frac{3}{2} ia^3 \alpha \alpha_1 \alpha_3 e^{ib} ccc \omega - \frac{3}{2} a^3 \alpha e^{ib} ccc - \alpha_2 \omega^4 \Omega_0^2 (e^{ib} a' + iae^{ib} b') + \alpha_2 \omega^2 (e^{ib} a' + iae^{ib} b') + \alpha_1 \alpha_3 \omega^2 (e^{ib} a' + iae^{ib} b') - i\omega^3 \Omega_0^2 (e^{ib} a' + iae^{ib} b') + i\omega (e^{ib} a' + iae^{ib} b') = 0 \tag{33}$$

where $ccc = 1 - \cos k$. Separating the real and imaginary parts yields the following equations

$$f + ga' + hab' = 0 \tag{34}$$

$$l - ha' + gab' = 0 \tag{35}$$

where $f, g, h,$ and l are defined as

$$g = -\frac{1}{2} \omega (\alpha_2 \omega (\Omega_0^2 (\bar{k} (\alpha_1 (-\text{Im}[\Gamma]) \text{Im}[K_\omega] + (\alpha_1 \text{Re}[\Gamma] - 2) \text{Re}[K_\omega] - 2) + 2\omega^2) - 2) + 2\Omega_0^2 \bar{k} \text{Im}[K_\omega] - \alpha_1 \alpha_3 \omega (\Omega_0^2 \bar{k} (\text{Re}[K_\omega] + 2) + 2)) \tag{36}$$

$$h = \frac{1}{2} \omega (\Omega_0^2 (\bar{k} (\text{Re}[K_\omega] (\alpha_1 \alpha_2 \text{Im}[\Gamma] \omega - 2) + \omega \text{Im}[K_\omega] (\alpha_2 (\alpha_1 \text{Re}[\Gamma] - 2) - \alpha_1 \alpha_3) - 2) + 2\omega^2) - 2) \tag{37}$$

$$f = \frac{3}{2} a^3 \alpha ccc (\omega^2 \Omega_0^2 - 1) \tag{38}$$

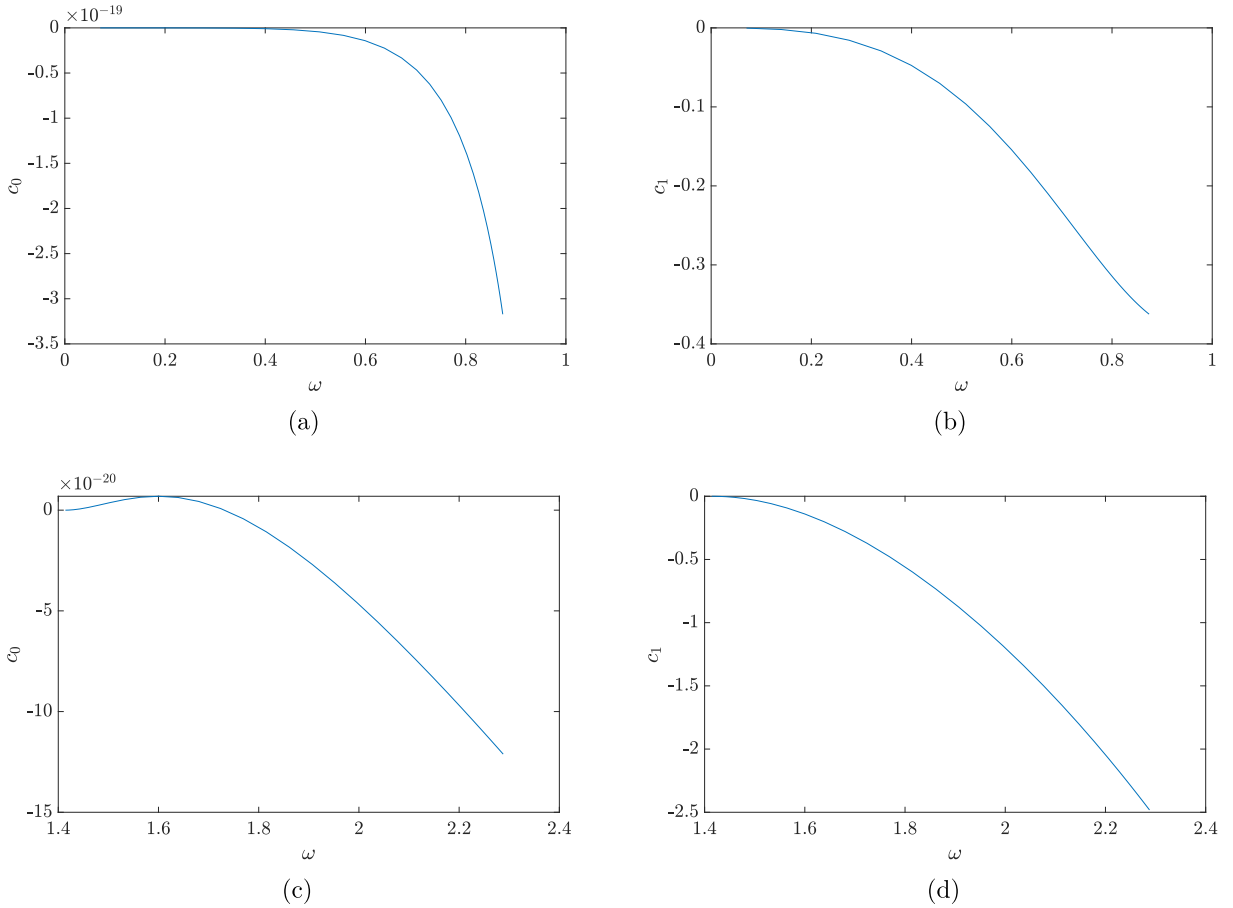


Fig. 2. Values of c_0 and c_1 over the frequency range (a)–(b): acoustic mode; (c)–(d): optical mode.

$$l = \frac{1}{2}(-3)a^3 \alpha c c c \omega (\alpha_2 (\omega^2 \Omega_0^2 - 1) - \alpha_1 \alpha_3) \quad (39)$$

It is noteworthy here that only f and l are function of vibration amplitude. One can solve Eqs. (34)–(36) to obtain

$$a' = \frac{lh - fg}{g^2 + h^2} \quad (40)$$

$$ab' = -\frac{gl + mh}{h^2 + g^2} \quad (41)$$

Therefore, the slow flow equations can be written in the following form

$$a' = c_0 a^3 \quad (42)$$

$$b' = c_1 a^2 \quad (43)$$

where c_0 and c_1 are constants. These slow flow equations are nonlinear and need to be solved in order to determine the correction term for the nonlinear frequency.

2.3. Approximate solution for slow flow equations

To obtain an approximate solution, we plot the values of c_0 and c_1 over the frequency range in Fig. 2 for $\epsilon\alpha = 0.06$, $\bar{k} = 1$, $\omega_n = \omega_d = 1000$ rad/s, $k_1 = 10^6$ N/m, $R = 100\Omega$, $\theta = 171 \times 10^{-12}$ N/V, and $C_p = 13.3 \times 10^{-9}$ F. One can observe that the values of c_0 are too small and almost negligible comparing to the values of c_1 in the acoustic and optical modes. This indicates

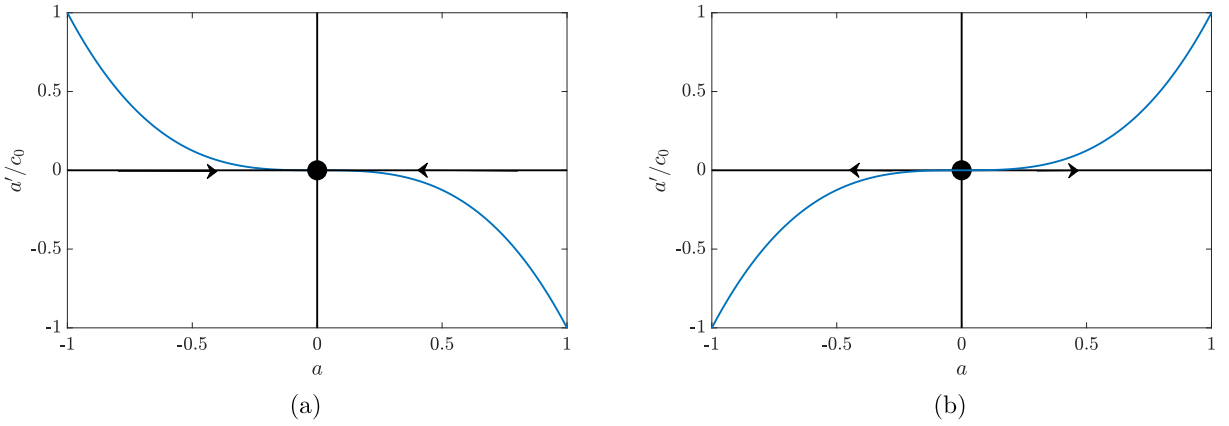


Fig. 3. Phase portrait of a' and a for different values of c_0 : (a): negative c_0 ; (b): positive c_0 .

that one can safely assume that $a' = 0$ and as a result the amplitude is constant $a = a_0$. Therefore, the correction factor can be written as

$$b' = c_1 a_0^2 \tag{44}$$

Integrating the differential equation yields

$$b = c_1 a_0^2 T_1 \tag{45}$$

and the nonlinear frequency can be written as

$$\omega_{nl} = \omega - \epsilon b' \tag{46}$$

For large c_0 , the amplitude can be determined as

$$a = \sqrt{\frac{-1}{2(c_0 T_1 + c)}} \tag{47}$$

where $c = \frac{-1}{2a_0^2}$. When c_0 is negative, the value under the square root is always positive; therefore, Eq. (47) is also a solution of the system for $T_1 > 0$. However, if c_0 is positive the square root has a solution only if $c_0 T_1 > \frac{1}{2a_0^2}$. Otherwise, the trivial solution is the only possible solution.

We plot the phase portrait for the first order system for positive and negative values of c_0 in Fig. 3. The results indicate that the stable solution associated with negative c_0 will reach 0 eventually; therefore, the trivial solution is always the only stable solution. On the other hand, the system departs from zero when c_0 is positive, which is not defined when $c_0 T_1 > \frac{1}{2a_0^2}$. Therefore, the system will also reach 0 eventually and only the trivial solution is stable.

3. Effect of electromechanical resonator on the band structure

In this section, we investigate the effect of the electromechanical coupling on the boundaries of the metastructure's bandgap. In particular, we fix the parameter of the metastructure and local resonator and we change the values of resistor unless mentioned otherwise. These parameter are defined as $\bar{k} = 1$, $\omega_n = \omega_d = 10^3$ rad/s, $k_1 = 10^6$ N/m, and $C_p = 13.3 \times 10^{-9}$ F. These parameters are chosen based on similar studies in Refs. [24,39].

3.1. Validation of the approximate analytical solution

To check the accuracy of the current analytical solution derived by the method of multiple scales, we first compare our results with those obtained for nonlinear chain in the absence of electromechanical coupling using the Lindstedt-Poincare method. This can be obtained by setting the load resistor and piezoelectric constant to zero. Therefore, the problem is reduced to the classical chain with mechanical resonators instead of electromechanical resonators. The comparison for both solutions are shown in Fig. 4-a. The results show a very good agreement with those in the literature.

Next, we consider the electromechanical coupling by shunting the system to a resistor. The analytical results here are validated numerically. We simulate a chain consisting of 500 cells, connected by nonlinear springs, and coupled to electromechanical resonators. The parameters of the chain are similar to those used in Fig. 4-a. The simulation is conducted by integrating the

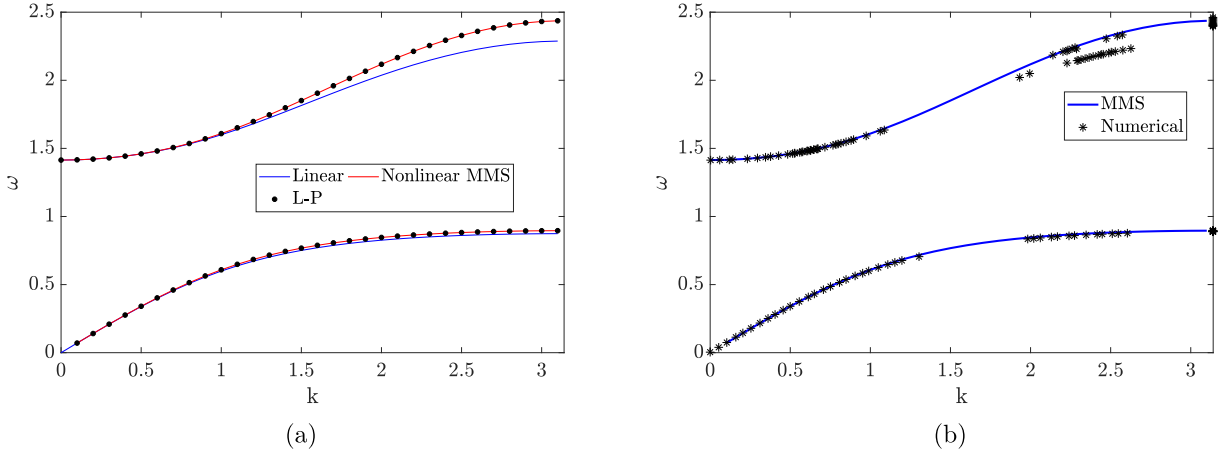


Fig. 4. Validation of the analytical results (a); without electromechanical coupling using [24]; (b); with electromechanical coupling using numerical simulations for $\theta = 10^{-10}$ N/V, $R = 10^4 \Omega$.

governing equation numerically by Matlab built-in solver ODE45. To omit any reflective waves, we apply Perfectly Match Layers (PML) at each end of the chain [20]. The chain is excited by a transient wave packet. We select the velocity of the wave packet to force the wave to propagate in one direction. This wave packet is defined as

$$u_m(0) = \frac{1}{2}(H(m-1) - H(m-1 - N_{cy}2\pi/k))(1 - \cos(mk/N_{cy})) \sin(mk) \quad (48)$$

$$\dot{u}_m(0) = \frac{1}{2}(H(m-1) - H(m-1 - N_{cy}2\pi/k))(-\omega_n \omega / N_{cy} \sin(mk/N_{cy}) \sin(mk) - \omega_n \omega (1 - \cos(mk/N_{cy})) \cos(mk)) \quad (49)$$

$$y_m(0) = K_\omega u_m(0) \quad (50)$$

$$\dot{y}_m(0) = K_\omega \dot{u}_m(0) \quad (51)$$

$$v = \Gamma K_\omega u_m(0) \quad (52)$$

where N_{cy} is the number of cycles and in our numerical simulations we set $N_{cy} = 7$, and $H(x)$ is the Heaviside function.

After simulating the system at any wavenumber, we determine the 2D Fourier transform (2DFFT) of the data in the frequency and wavenumber domains. Then the natural frequency of the system is the frequency associated with the maximum power density point. By sweeping the wave number over the first Brillouin zone, one can numerically reconstruct the dispersion curves from the obtained sets of wavenumbers and frequencies. It is noteworthy here that each of the optical and acoustic modes can be obtained separately by exciting the system at frequencies close to the required mode frequencies.

We plot the numerical dispersion curves in Fig. 4-b. The numerical results also show a good agreement with the analytical results in the presence of the electromechanical coupling. However, the analytical solution fails to predict the middle branch of the optical mode. In this region, there is a significant frequency shift (as we will show in the subsequent sections) associated with transient wave packets excitation. This region is called Pseudo-bandgap [24].

3.2. Linear band structure

When the problem is linear, we plot the dispersion curves with and without electromechanical coupling in Fig. 5. Unlike the chain with damping [40], it can be observed that shunting the electromechanical resonator to a load resistor does not affect the band structure of the metastructure for the weak electromechanical coupling case as shown in Fig. 5-a. Hence, harvesting the power has no role in controlling the boundary of the bandgap although it may change the attenuation level inside the bandgap (see Fig. 5-b). This indicates that metastructures can be used for simultaneous energy harvesting and vibration mitigation without degrading the bandgap boundary when the electromechanical coupling is weak.

For larger electromechanical coupling values up to $\theta = 10^{-3}$ N/V, the electromechanical coupling has also no noticeable effect on the band structure for different shunted load resistors. However, for $\theta \geq 10^{-2}$ N/V the band structure starts deforming and emerging into one dispersion curve branch instead of two as shown in Fig. 5-c. Therefore, the bandgap disappears at this level of electromechanical coupling. Moreover, the shunted resistor has a significant role in the dispersion curve shape at this level of electromechanical coupling as shown in Fig. 5-d.

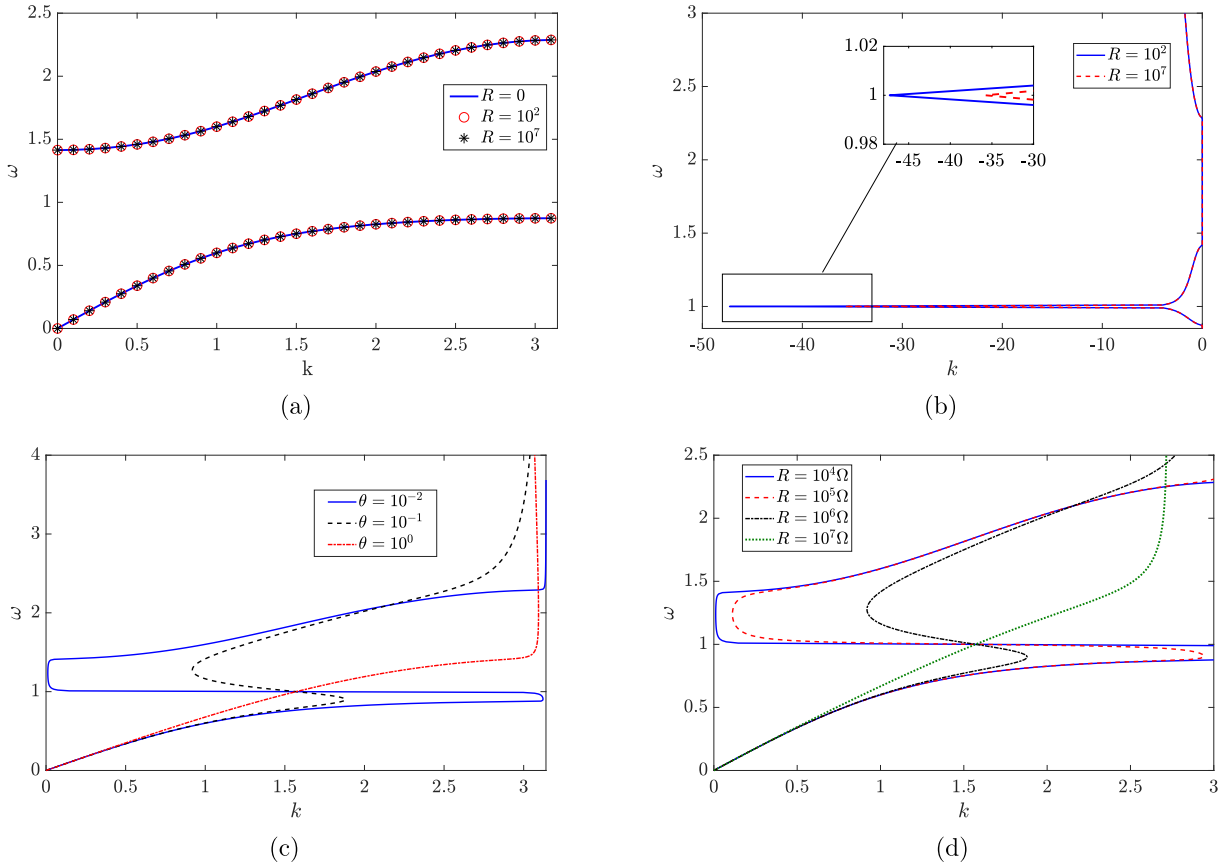


Fig. 5. The effect of electromechanical coupling on the band structure in linear chain. (a): Weak electromechanical coupling $\theta = 10^{-10}$ N/V; (b): Imaginary part of the band structure $\theta = 10^{-10}$ N/V; (c): Strong electromechanical coupling values when $R = 10^2\Omega$; (d): Effect of resistor on strong electromechanical coupling, $\theta = 10^{-2}$ N/V.

3.3. Nonlinear band structure

When the problem is nonlinear, we first plot the dispersion curves in the absence of electromechanical coupling for different types of nonlinearities in Fig. 6-(a). It can be observed that hardening nonlinearity shifts the dispersion curves up while softening nonlinearity shifts the curves down. Moreover, this shift is more significant in the optical mode. Next, we plot the dispersion curves with electromechanical coupling in Fig. 6-(b)-(f). For both types of nonlinearities (hardening and softening) with weakly electromechanical coupling (Fig. 6-(b) and (c)), it can be revealed that the effect of electromechanical coupling is negligible on the bandgap boundaries and only the nonlinearity in the chain shifts them. Therefore, one can also use metastructures for simultaneous energy harvesting and vibration reduction when the chain is nonlinear without affecting the bandgap boundaries. It is noteworthy here that these observations only hold for electromechanical coupling coefficient of $10^{-10} < \theta < 10^{-3}$ N/V. Similar to the linear case, stronger electromechanical coupling (i.e., $\theta \geq 10^{-3}$ N/V) also alters the band structure of nonlinear systems as shown in Fig. 6-(d) and (e). Moreover, the band structure for θ ranging between 10^{-3} and 10^0 N/V significantly depends on the shunted resistor unlike the case of weakly electromechanical coupling.

In the subsequent sections, our study will focus on the weakly electromechanical coupling case because θ depends on the piezoelectric constant which is usually at the order of 10^{-10} for most engineering applications [39].

4. Spectro-spatial analysis

In the previous section, we showed that weakly electromechanical coupling has no effect on the band structure in both linear and nonlinear chains. Nevertheless, the nonlinearity in the chain shifts the dispersion curves up or down depending on the type of nonlinearity. However, the dispersion characteristics do not reveal enough detailed information about nonlinear wave propagation phenomena except frequency shifts. Therefore, we employ the spectro-spatial analysis in this section to demonstrate other nonlinear wave propagation phenomena, particularly, wave distortion represented by wave localization or wave dispersion in nonlinear medium. This is done by analyzing the numerical data by different signal processing tools as it will be shown in the subsequent subsections.

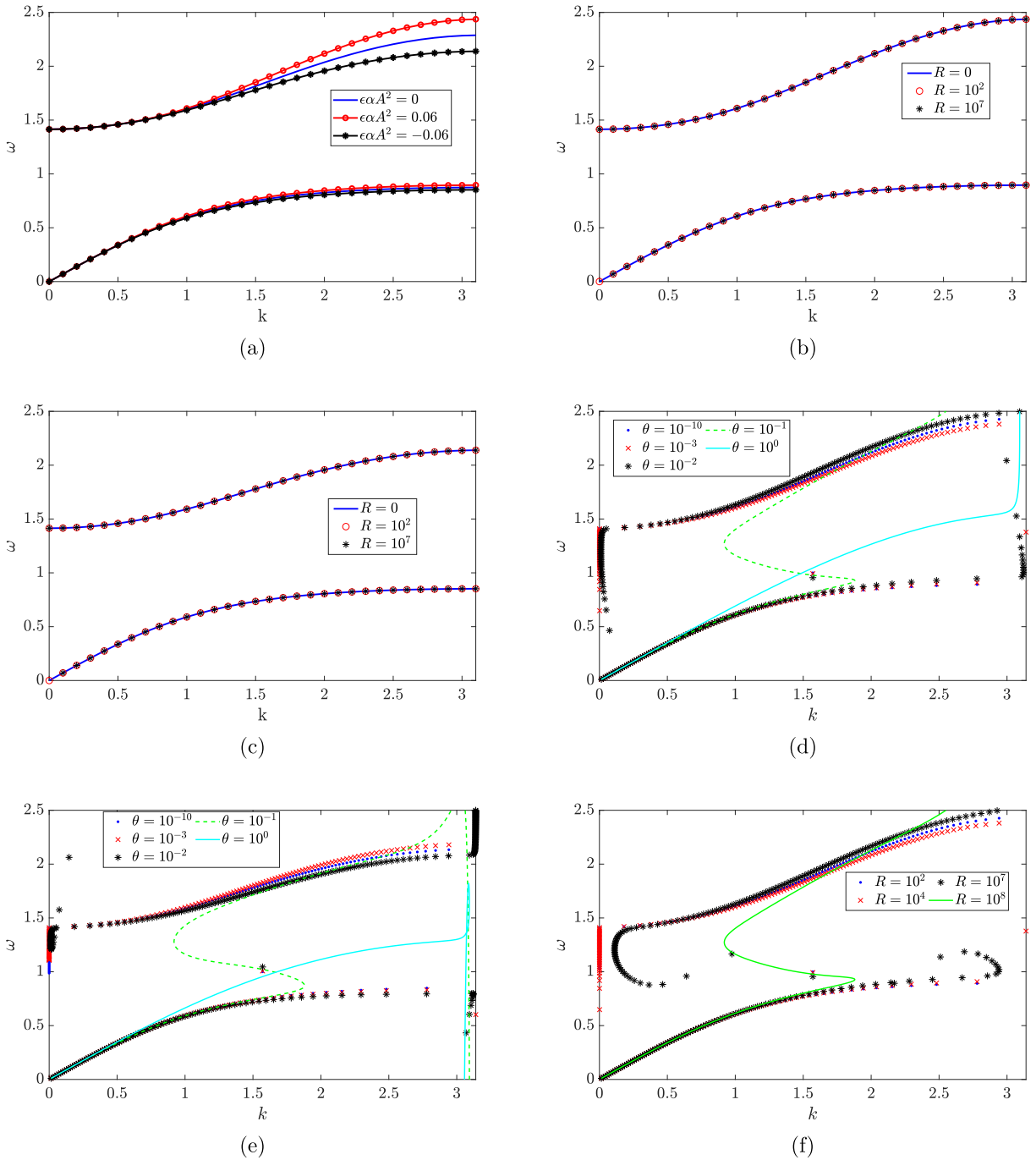


Fig. 6. The effect of electromechanical coupling on the band structure in nonlinear chain. (a): In the absence of electromechanical coupling; (b): Hardening nonlinearity with weakly electromechanical coupling $\theta = 10^{-10}N/V$; (c): Softening nonlinearity with weakly electromechanical coupling $\theta = 10^{-10}N/V$; (d): Hardening nonlinearity with strong electromechanical coupling $R = 10^4\Omega$; (e): Softening nonlinearity with strong electromechanical coupling $R = 10^4\Omega$; (f): Effect of resistor on strong electromechanical coupling, $\theta = 10^{-3}N/V$.

4.1. Spatial profile of the wave packet

The wave profile of the output voltage and the voltage in the input cell is plotted in Figs. 7–8 for different load resistors and different wave limits. It should be noted that the input voltage is determined using Eq. (52) and the output voltage is calculated using numerical integration. Considering the acoustic-mode wave in the long wavelength region, Fig. 7-a shows that the harvested power decays through the chain for both linear and hardening nonlinear chains. This is not surprising since the

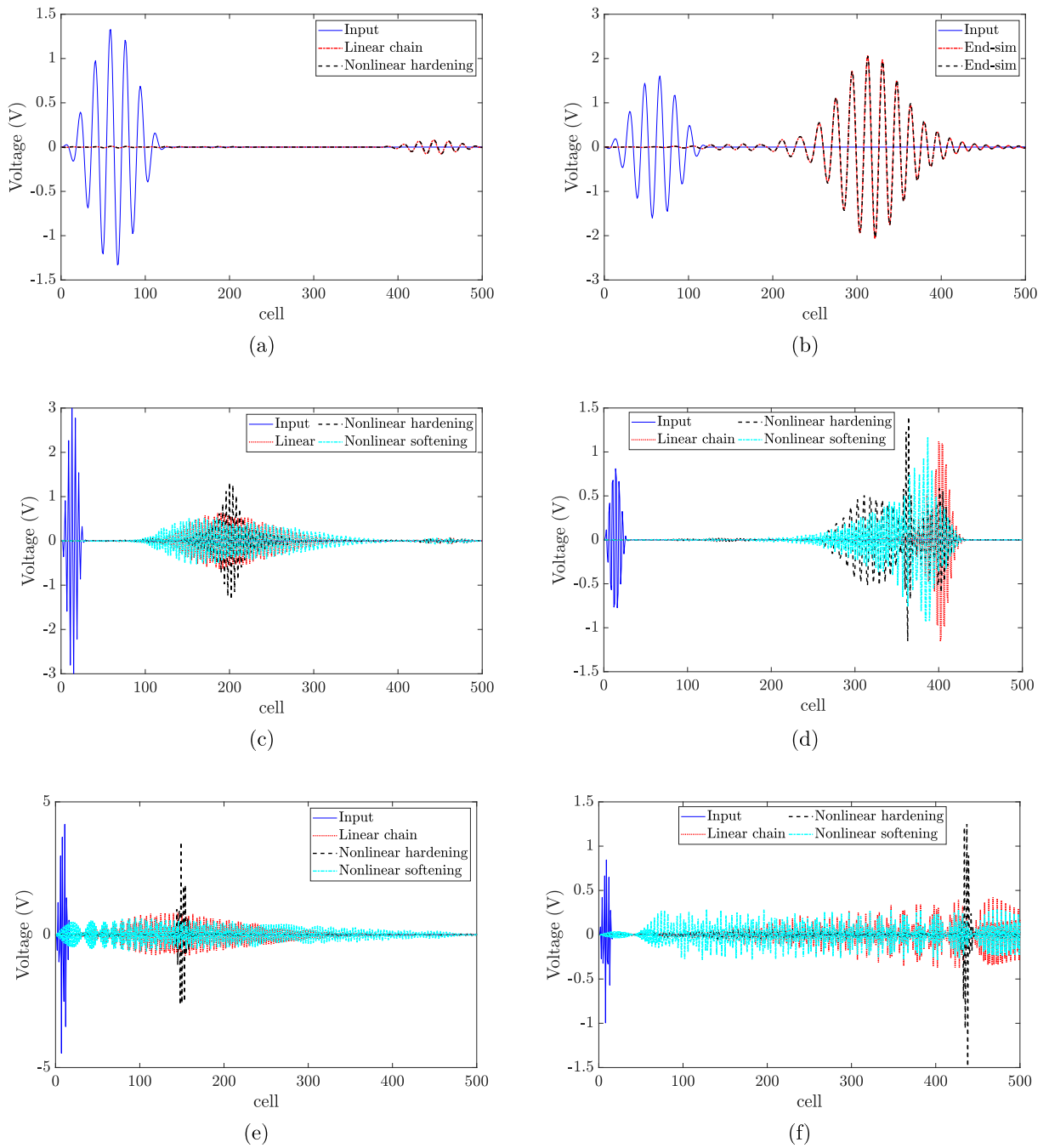


Fig. 7. Spatial profile of the wave packet of harvested voltage from electromechanical resonator, $R = 10^7 \Omega$, $\theta = 10^{-8} \text{ N/V}$; (a): $k = \pi/9$ acoustic mode, (b): $k = \pi/9$ optical mode, (c): $k = \pi/2$ acoustic mode, (d): $k = \pi/2$ optical mode, (e): $k = 7\pi/9$ acoustic mode, (f): $k = 7\pi/9$ optical mode.

frequency of the wave packet is away from the electromechanical resonator frequency. This figure is a mirror image of the wave profile of a wave propagating in a nonlinear chain since the effect of nonlinearity is negligible in the long wavelength limit. However, at frequencies close to the resonator frequency in the long wavelength limit (optical mode), the harvested voltage wave propagates through the structure as shown in Fig. 7-b. Yet the nonlinearity is negligible in this wavelength limit of the optical branch.

For the acoustic branch in the medium wavelength domain (Fig. 7-c), the dispersion curve is nonlinear (i.e., variable slope) and hence as expected, the wave is dispersive and its amplitude decreases significantly when the chain is linear. For the hardening nonlinear chain, the wave is split into two components; one is dispersive with low amplitude and the other is localized with high amplitude (solitary) wave. The solitary wave obtained from the nonlinear chain exhibits the highest output voltage

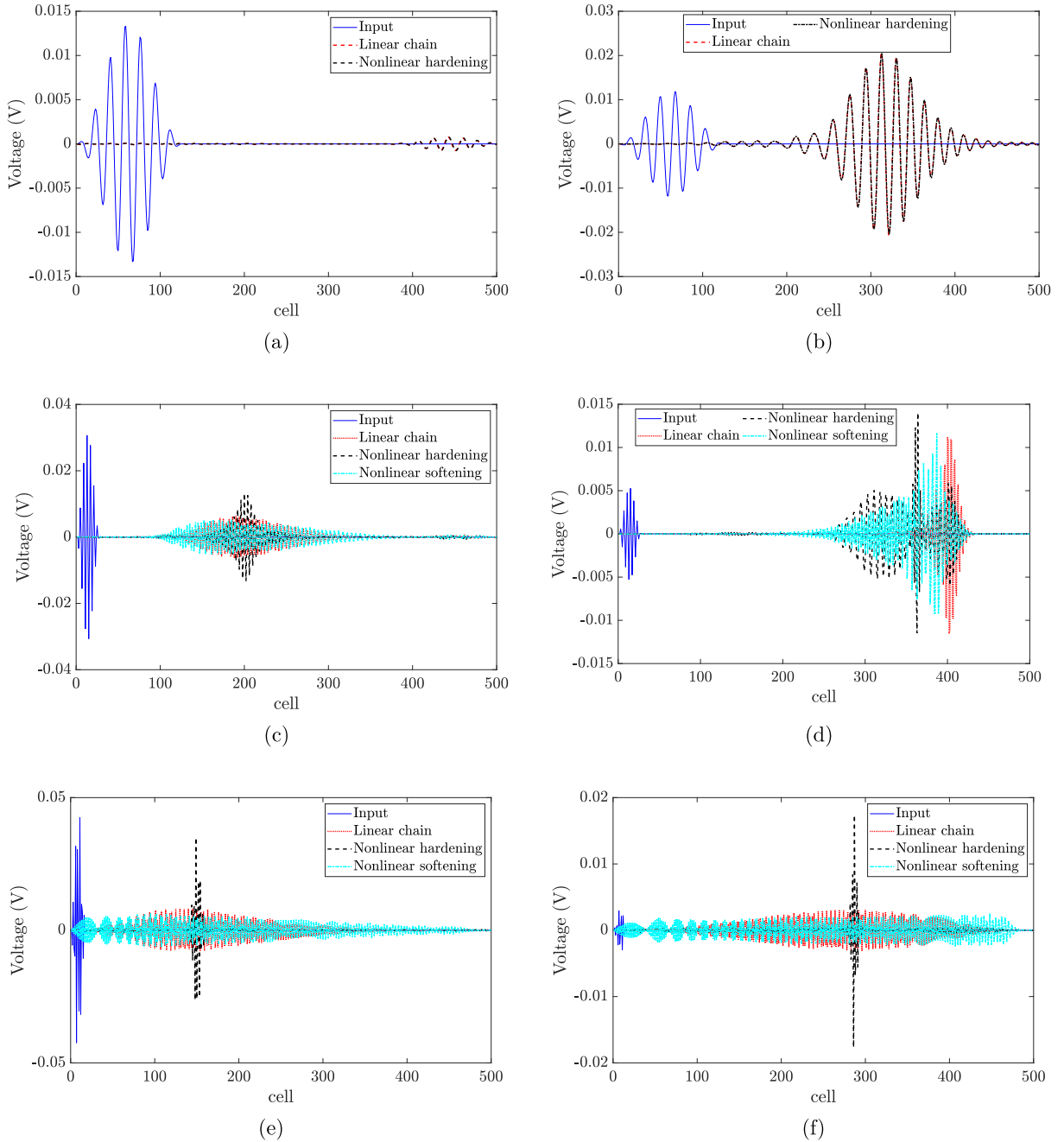


Fig. 8. Spatial profile of the wave packet of harvested voltage from electromechanical resonator, $R = 10^7 \Omega$, $\theta = 10^{-10}$ N/V; (a): $k = \pi/9$ acoustic mode, (b): $k = \pi/9$ optical mode, (c): $k = \pi/2$ acoustic mode, (d): $k = \pi/2$ optical mode, (e): $k = 7\pi/9$ acoustic mode, (f): $k = 7\pi/9$ optical mode.

as compared to the linear and softening nonlinear chains. The softening nonlinear chain stretches the dispersive wave, thus resulting in the lowest output voltage as compared to the linear and nonlinear hardening chains. Nevertheless, the number of cells engaged in energy harvesting at specific time are higher than those in the linear and hardening nonlinear chains.

For the optical mode in the medium wavelength limit, Fig. 7-d shows that the wave still has two different magnitude components for the hardening nonlinearity case, but the output voltage of the localized wave is not significantly higher than that of the linear chain. Yet the higher amplitude component in hardening nonlinearity in this case is more localized than that of the acoustic mode wave of Fig. 7-c. Fig. 7-d also shows that the softening nonlinear chain lowers the amplitude of the localized component and stretches the other wave component over more cells.

In the short wavelength region (Fig. 7-e for the acoustic mode and Fig. 7-f for the optical mode), it can be noted that the linear wave is more dispersive since the dispersion curve in this region is strongly nonlinear (refer to Section 4.3 for more details). However, the effect of nonlinearity is more significant in localizing the wave for the hardening nonlinearity case and stretching the wave for the softening nonlinearity case. These results suggest that higher power amplitude solitary waves are developed when the nonlinearity is hardening while more cells are engaged in energy harvesting when the nonlinearity is softening.

Finally, we show the spatial profile of the harvested voltage due to wave packet excitation at lower electromechanical coupling in Fig. 8. The general observations discussed for the case of $R = 10^7 \Omega$ and $\theta = 10^{-8}$ N/V holds here. However, some of the spatial profiles are slightly different, especially for the acoustic mode in the long wavelength limit. This indicates that the load resistor has a slight effect on the spatial profile of the wave propagation.

4.2. Spatial short term fourier transform of wave motion

In this section, we plot the short term Fourier transform (STFT) to investigate the change in wave characteristics over time in the space domain as depicted in Figs. 9 and 10 for the acoustics and optical modes, respectively. We use a Hann window with the size of input burst to contain the short spatial components over time. This Hann window is represented by a signal between dashed lines in the figures. It is noteworthy here that we only consider medium and short wave lengths in this section since the previous section revealed that nonlinearity has no effect in the long wave length domain. These analyses are carried out on a chain coupled to $R = 10^7 \Omega$ load resistors.

For the acoustic-mode wave propagating in a linear chain (Fig. 9-a for $k = \pi/2$ and Fig. 9-b for $k = 7\pi/9$), the voltage output is dispersive and has only one component with low amplitude. Moreover, it can be observed that the stretching of the wave is more severe at shorter wavelengths. It should be noted here that we plot the input signal in addition to the output signal; therefore, the reader can recognize the wave distortion. Furthermore, for better visualization of the output signal amplitude, we can compare the ratio between the output to the input signal to demonstrate the increase or decrease in wave amplitude. For instance, output voltage wave amplitude in Fig. 9-b is lower than that in Fig. 9-a since the input signal in the former case is lower.

For the nonlinear chain, two different behaviors are observed for different types of nonlinearities. For hardening nonlinearity (Fig. 9-c for $k = \pi/2$ and Fig. 9-d for $k = 7\pi/9$), solitary waves are developed, thus the output voltage is higher and localized within a few number of cells. However, the effect of hardening nonlinearity is more significant in the shorter wavelength limit and some of its energy is shifted outside the Hann window limits as shown in Fig. 9-d. For softening nonlinearity (Fig. 9-e for $k = \pi/2$ and Fig. 9-f for $k = 7\pi/9$), the output voltage wave is stretched over the chain. This wave has lower amplitude than the linear case. It is also observed here that the effect of nonlinearity becomes more significant with reducing the wavelength. Moreover, some of the energy content is shifted below the Hann window limits. In general, we observe that the output voltage wave is attenuated through the chain at all wavelength regions of the acoustic mode; however, wave amplitude is almost at the same order of magnitude of the input wave amplitude in hardening nonlinear chain at short wavelength.

For the optical mode wave, we show STFT in Fig. 10. In general, the output voltage wave propagates at higher amplitudes through the chain in all wavelength limits. Yet this propagation depends significantly on the type of nonlinearity and wavelength. For a wave propagating in a linear chain at medium wavelength (Fig. 10-a), it can be observed that the wave is not dispersive and has a significant amplitude localized wave unlike the behavior observed in the same wavelength region of the acoustic mode. However, the wave is clearly dispersive at shorter wavelengths as depicted in Fig. 10-b for the linear chain.

For the optical branch in the medium wavelength region, (Fig. 10-c and d), the output voltage wave is severely distorted and brakes down into multiple components. For hardening nonlinearity, the output wave has three components. The first component has low wavenumber and the wave is dispersive with low amplitude. The second component lies inside the Hann window (linear limit) and the wave is also dispersive. As for the third component, most of the energy content is shifted above the Hann window due to hardening nonlinearity. The latter represents a solitary wave. For softening nonlinearity (Fig. 10-d), the output voltage wave is broken into two components. The first component has a high wavenumber and the wave is dispersive with low amplitude. However, most of the energy of the linear wave is significantly shifted below the Hann window. In both types of nonlinearity, we observe a significant frequency shift for the optical branch in the medium wavelength limit since most of the output energy dilates outside the input signal frequency confined within the Hann window.

Finally, we investigate the wave distortion for the optical branch in the short wavelength domain (Fig. 10-e and f). The results indicate that the behavior of this mode is similar to that of the acoustic mode in the short wavelength limit. The hardening nonlinearity develops a localized solitary wave, which has a voltage amplitude much higher than the linear case as shown in Fig. 10-e. On the other hand, softening nonlinearity stretches the wave significantly in this wavelength limit. The resulting wave is dispersive with low amplitude. It is noteworthy here that, for the nonlinear chain, some of the energy content is shifted outside the limits of the input signal in the short wavelength region.

4.3. Contour plots of 2D fourier transform

After analyzing the output voltage of the wave characteristics over time in the spatial domain, we investigate the frequency-wavenumber characteristics of the system in order to reconstruct the nonlinear dispersion curves and examine the Pseudo-bandgap observed in Fig. 4-b. This can be done by determining the 2D Fourier transform for the temporal and spatial compo-

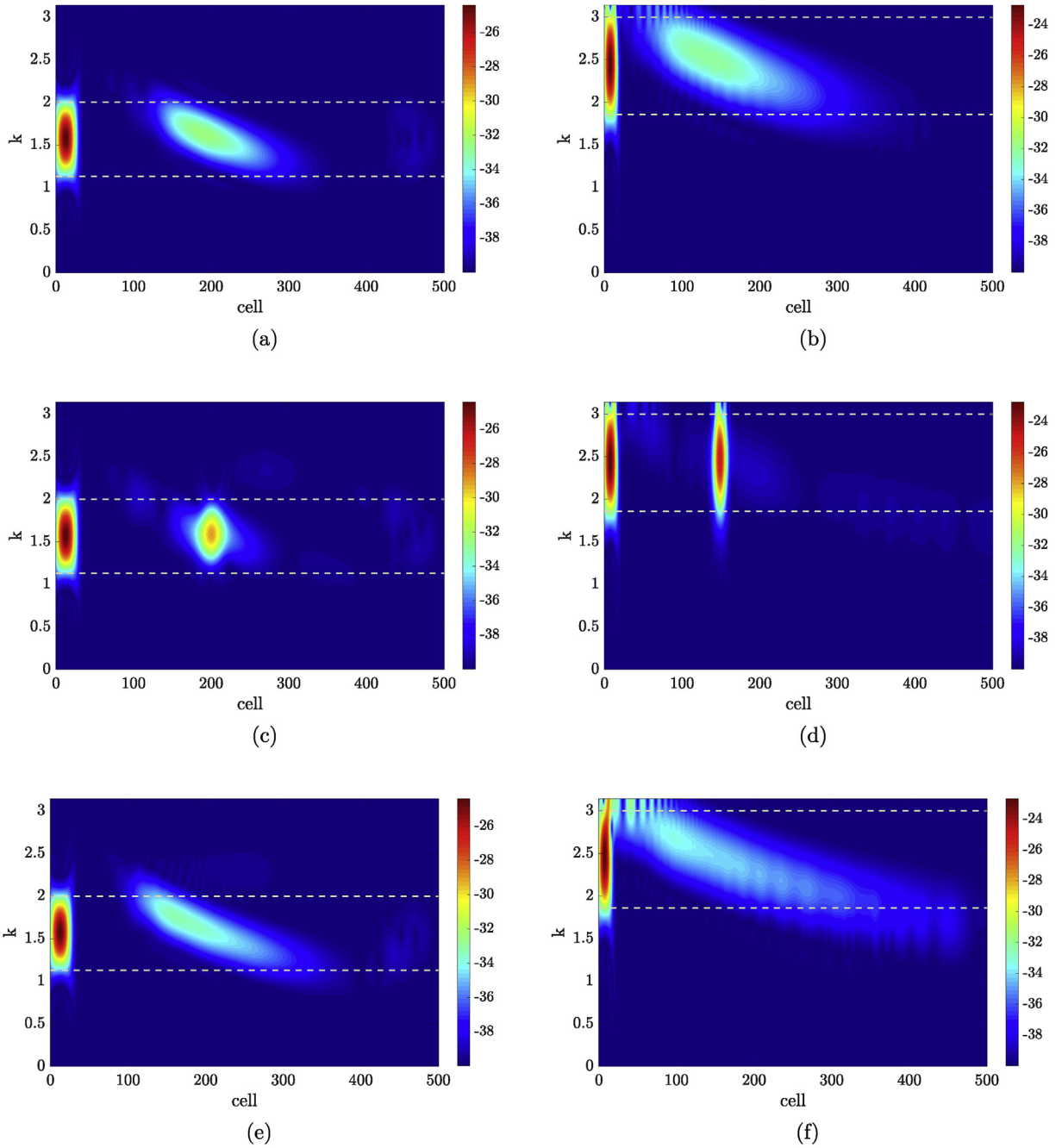


Fig. 9. Short term Fourier transform for energy harvested in acoustic mode and for different types of nonlinearity, $R = 10^7 \Omega$, $\theta = 10^{-10}$ N/V; (a): $k = \pi/2$, $\epsilon\alpha A^2 = 0$, (b): $k = 7\pi/9$, $\epsilon\alpha A^2 = 0$, (c): $k = \pi/2$, $\epsilon\alpha A^2 = 0.03$, (d): $k = 7\pi/9$, $\epsilon\alpha A^2 = 0.03$, (e): $k = \pi/2$, $\epsilon\alpha A^2 = -0.03$, (f): $k = 7\pi/9$, $\epsilon\alpha A^2 = -0.03$.

nents. We plot the contour lines of the results in frequency-wavenumber domain for the acoustic mode in Fig. 11 and optical mode in Fig. 12. To compare the distribution of the frequency-wavenumber component for different types of nonlinearity, we plot the output voltage power density with the same wavelength inside the same frequency-wavenumber band limit. We focus only on waves propagating in the medium and short wavelength regions since we have shown that the effect of nonlinearity is negligible in the long wavelength limit.

For the acoustic mode in the medium wavelength limit (Fig. 11-a, b, and c), it is demonstrated that the hardening nonlinearity localized the output voltage power spectrum while the softening nonlinearity stretches it over a wider range of frequency-wavenumber. Moreover, it can be demonstrated that hardening nonlinearity bends the nonlinear dispersion curve (Fig. 11-a) to a less nonlinear dispersion curve while the softening nonlinearity bends the nonlinear dispersion curve to a more nonlinear

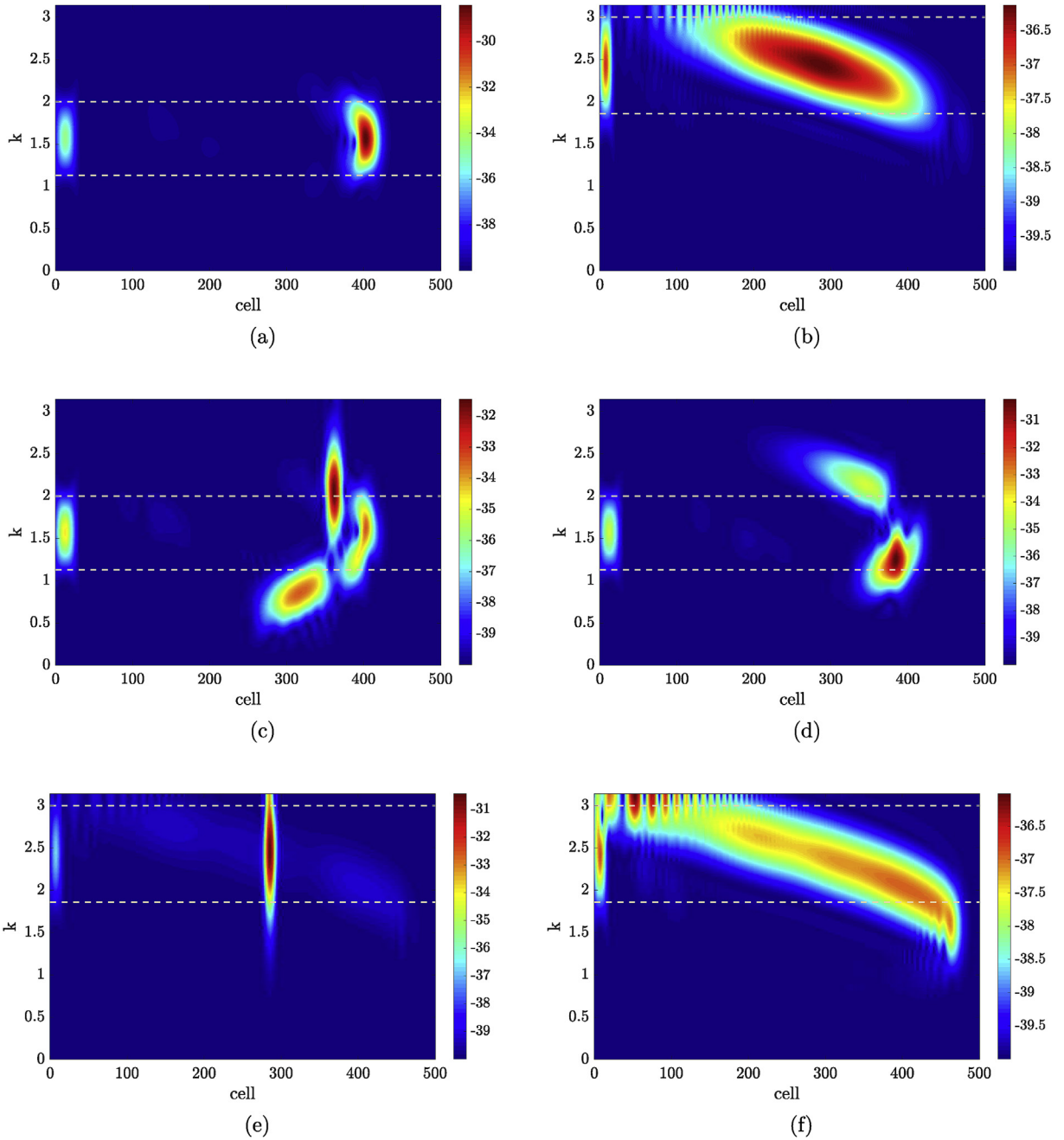


Fig. 10. Short term Fourier transform for energy harvested in optical mode and for different types of nonlinearity, $R = 10^7\Omega$, $\theta = 10^{-10} N/V$; (a): $k = \pi/2$, $\epsilon\alpha A^2 = 0$, (b): $k = 7\pi/9$, $\epsilon\alpha A^2 = 0$, (c): $k = \pi/2$, $\epsilon\alpha A^2 = 0.03$, (d): $k = \pi/2$, $\epsilon\alpha A^2 = -0.03$, (e): $k = 7\pi/9$, $\epsilon\alpha A^2 = 0.03$, (f): $k = 7\pi/9$, $\epsilon\alpha A^2 = -0.03$.

dispersion curve; therefore, the wave becomes more dispersive. It is noteworthy that no significant frequency shift can be observed. For the same mode, but in the short wavelength region (Fig. 11-d, e, and f), similar behavior in localizing and stretching the power spectrum can be observed. However, the effect here is more significant. For instance, the power spectrum in the case of hardening nonlinearity is almost linear which indicates the birth of solitons. On the other hand, power spectrum curves are more nonlinear in the case of softening nonlinear chain.

Next, we investigate the contour plots of 2D Fourier transform for the optical mode (Fig. 12). For the medium wavelength limit (Fig. 12-a, b, and c), we observe a significant frequency-wavenumber shift in the power spectrum contours for both types of nonlinearity. However, this shift is more pronounced in the case of hardening nonlinearity. It can be observed that the power spectrum is broken into mainly three components in the case of hardening nonlinearity while it is divided into two components

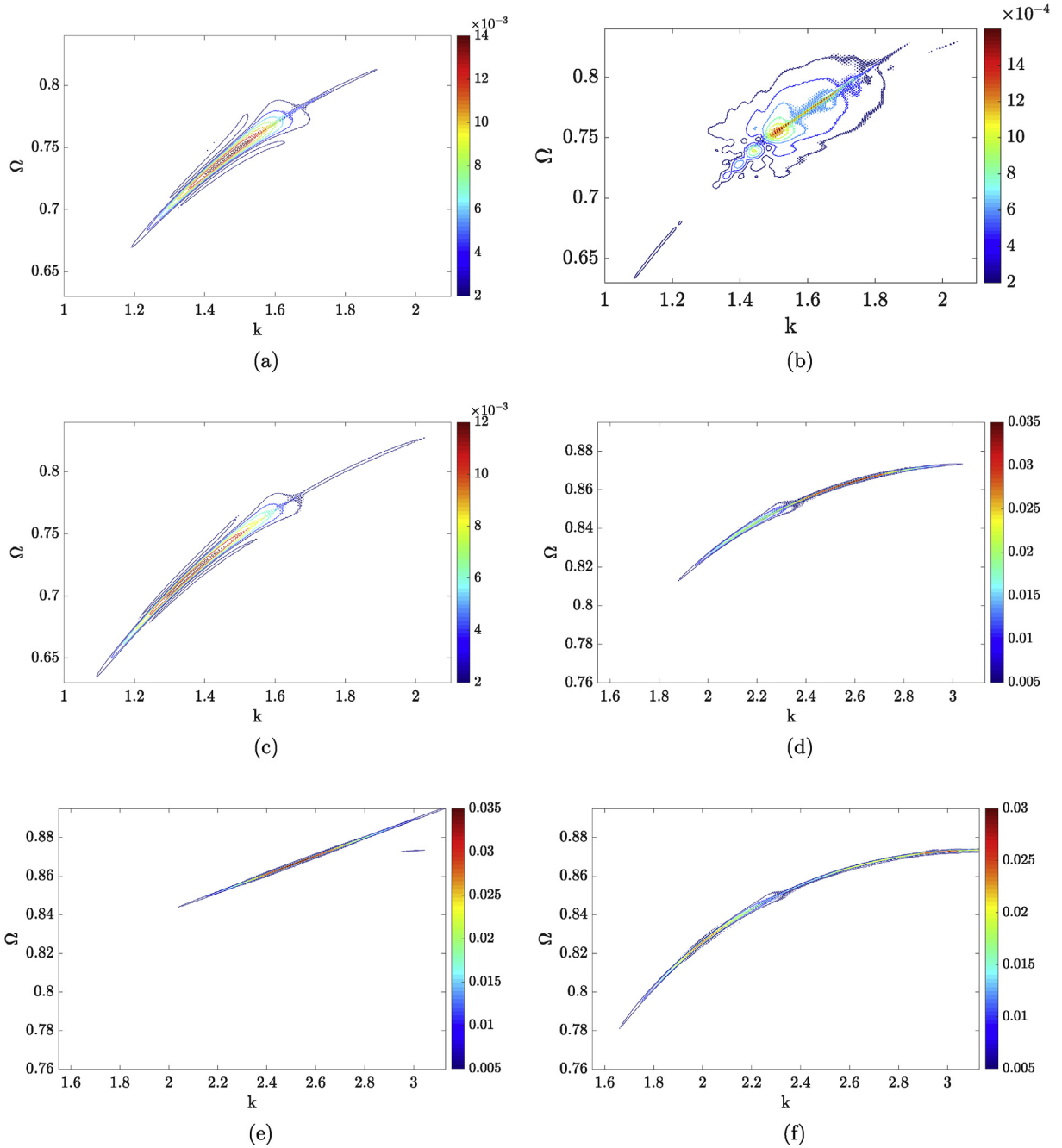


Fig. 11. 2D Fourier transform for harvested voltage in acoustic mode, $\theta = 10^{-10}$ N/V, $R = 10^7 \Omega$; (a): $k = \pi/2, \epsilon\alpha A^2 = 0$, (b): $k = \pi/2, \epsilon\alpha A^2 = 0.03$, (c): $k = \pi/2, \epsilon\alpha A^2 = -0.03$, (d): $k = 7\pi/9, \epsilon\alpha A^2 = 0$, (e): $k = 7\pi/9, \epsilon\alpha A^2 = 0.03$, (f): $k = 7\pi/9, \epsilon\alpha A^2 = -0.03$.

in the case of softening nonlinearity. This is not surprising since we have observed this broken signal in STFT plots in the previous section. In Fig. 12-b, it is observed that the higher frequency component has most of the energy content; moreover, this component has a linear dispersion curve (i.e., constant slope), which indicates that there is a development of solitary wave. For the short wavelength limit (Fig. 12-d, e, and f), a frequency-wavenumber shift is also observed in the presence of nonlinearity; however, neither significant shift nor severe wave distortion is demonstrated in this wavelength region. When the chain has hardening nonlinearity (Fig. 12-e), the power spectrum of the output voltage is concentrated in a linear dispersion curve (strong soliton) and shifted to higher frequency values. Nevertheless, one can still observe some of the energy content appearing as nonlinear dispersion curves similar to those observed in the case of linear chain shown in Fig. 12-a. For softening nonlinearity

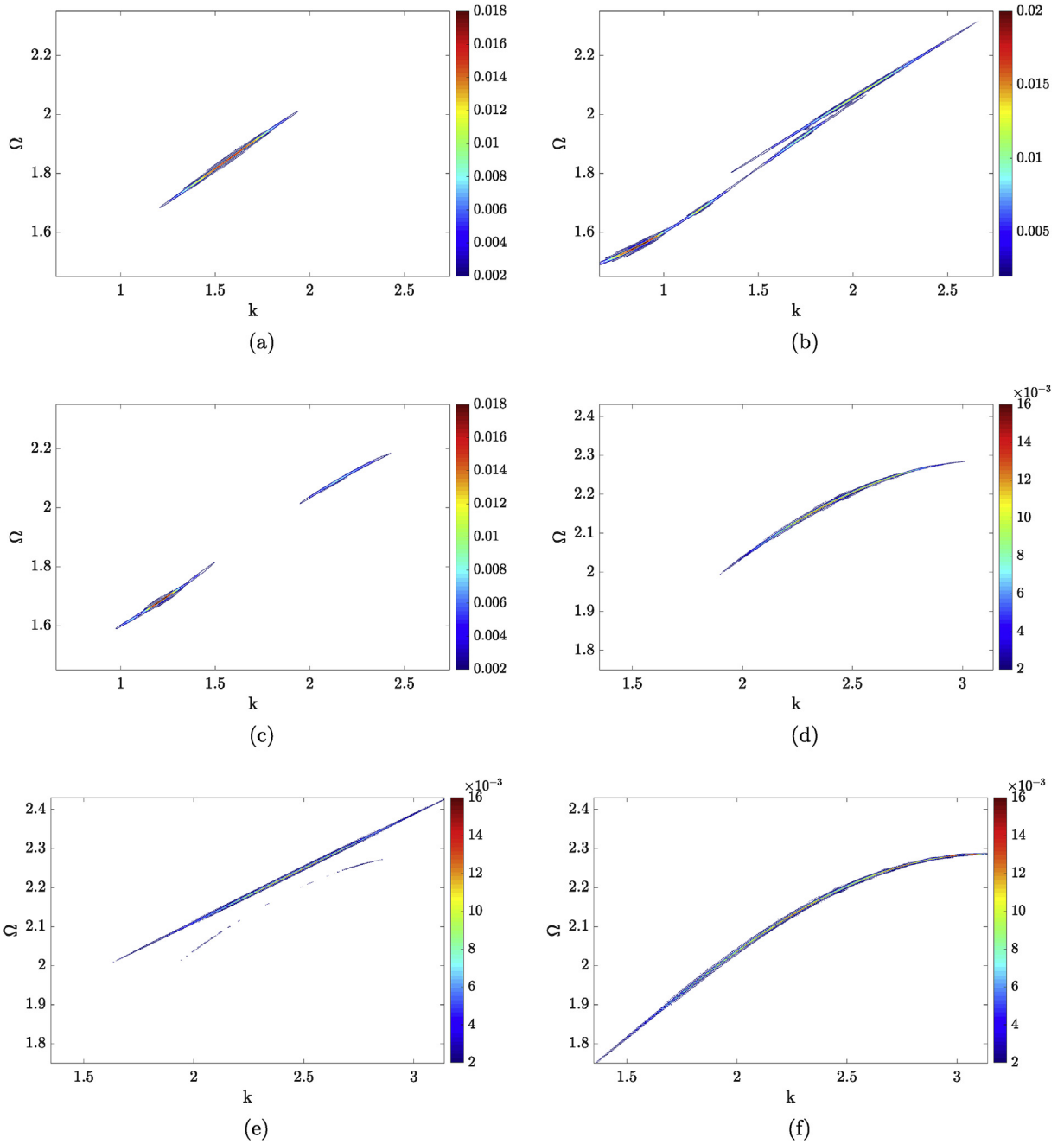


Fig. 12. 2D Fourier transform for harvested voltage in optical mode, $\theta = 10^{-10}$ N/V, $R = 10^7 \Omega$; (a): $k = \pi/2, \epsilon\alpha A^2 = 0$, (b): $k = \pi/2, \epsilon\alpha A^2 = 0.03$, (c): $k = \pi/2, \epsilon\alpha A^2 = -0.03$, (d): $k = 7\pi/9, \epsilon\alpha A^2 = 0$, (e): $k = 7\pi/9, \epsilon\alpha A^2 = 0.03$, (f): $k = 7\pi/9, \epsilon\alpha A^2 = -0.03$.

Fig. 12-f, the power spectrum is shifted to lower frequency values. However, the energy content is not broken into multiple components, instead the signal is almost concentrated in one branch over wider band of frequency and wavenumber.

5. Discussion

Finally, we add some general comments about simultaneous energy harvesting or sensing and vibration attenuation in non-linear metastructures based on the analyses carried out in the present study. The output voltage wave propagates to higher level through the chain only for the optical branch. However, the wave amplitude can be at the same level of input signal when the chain has hardening nonlinearity for the acoustic mode in the short wavelength limit. This is because solitary wave can be

observed in this limit. The hardening nonlinearity can also convert the dispersive waves to solitary waves with higher voltage amplitude in the optical mode. On the other hand, softening nonlinearity stretches the voltage wave over the chain and reduces the amplitude. Therefore, higher voltage amplitude wave is predicted with hardening chain while lower voltage amplitude is predicted with softening chain. However, the number of cells engaged in energy harvesting is higher in the latter case. Nonlinear chains also shift the output signal frequency to higher or lower values at medium and short wavelengths when the nonlinearity is hardening or softening, respectively. However, this shift is significant for the optical mode in the medium wavelength limit. This significant shift is concentrated in shifting the higher power density component up or down while other lower value components can also be observed at different frequencies.

Nonlinear chains can be employed toward better simultaneous energy harvesting, sensing, and vibration attenuation. For instance, the significant increase in the voltage amplitude by hardening chain allows better and faster sensing of the input disturbance. In addition, the significant frequency shift can be utilized to design electromechanical rectifier [16]. This can be achieved by coupling such a nonlinear electromechanical chain with a linear electromechanical chain and tuning the frequency shift region to the bandgap of the linear chain. This will allow energy harvesting (sensing) and wave propagation in only one direction.

Finally, replacing some of the local electromechanical resonators by local mechanical resonators should preserve the performance of vibration attenuation in the structure. This is because the weak electromechanical coupling has no effect on the size of the bandgap. However, these local mechanical resonators must have equivalent dynamical properties as those of the local electromechanical resonators. Thus, only finite number of energy harvester can be considered. This will be more meaningful from the prospective of energy harvesting.

6. Conclusion

In this work, a nonlinear metastructure coupled to a linear electromechanical resonator was studied. The metastructure was modeled as a chain of masses connected by weakly nonlinear springs. The cells were coupled to electromechanical resonators, which were also modeled as a spring-mass system and shunted to a load resistor. We employed the method of multiple scales to derive an analytical approximate solution for the nonlinear dispersion relations. These expressions were validated by direct numerical integration. The validation showed that the method of multiple scales can accurately predict the cut-off frequencies, but not the significant frequency shift in the medium wavelength limit of the optical branch. The analytical results indicated that neither the band structure of linear nor nonlinear chains were affected by the weakly electromechanical coupling. These findings suggest that energy harvesting does not degrade the vibration mitigation limits in metastructures. However, for very strong electromechanical coupling, the electromechanical coupling can alter the band structure. Nevertheless, these values of coupling coefficient are much higher than those in real life engineering applications.

We further investigated the nonlinear voltage output wave propagation by studying the spectro-spatial features using different signal processing techniques. This provided further detailed information about different nonlinear phenomena based on the type of nonlinearity. The spatial profile of the output voltage wave demonstrated that the wave does not propagate for higher values comparing to input wave profile in linear chains. The effect of nonlinearity in nonlinear chains appeared as wave stretching in softening chains or wave localization in hardening chains. It was demonstrated that an acoustic-mode wave in the short wavelength region can propagate with higher voltage amplitude only for the hardening nonlinear chain. Conversely, an optical-mode wave in all wavelength regions can propagate with high voltage amplitude in both linear and nonlinear chains. Yet softening nonlinearity can stretch the wave while hardening nonlinearity can localize it. This wave distortion significantly depends on the wave length. The images of STFT demonstrated the output voltage wave distortion due to nonlinearity. The results indicated that there is a significant frequency shift at frequency-wavenumber located in the middle of the optical mode. Moreover, it was shown that the wave gets divided into multiple components in the medium wavelength limit. Furthermore, the spectro-spatial analysis revealed that the nonlinear dispersion curves can be reconstructed by a contour of 2D Fourier transform. These contour plots demonstrated the birth of solitary waves in hardening nonlinear metastructures at medium and short wavelengths.

Finally, the observed significant frequency shift by spectro-spatial analysis in nonlinear metastructures can be employed to construct electromechanical diodes with simultaneous uni-direction energy harvesting and energy transfer.

Author contribution statement

Mohammad Bukhari, Conceptualization, Methodology, Software, Validation, Formal analysis, Investigation, Writing - Original Draft, Visualization. Oumar Barry, Conceptualization, Methodology, Investigation, Resources, Writing - Review & Editing, Visualization, Supervision, Project administration, Funding acquisition.

Acknowledgment

This work was supported by the start-up grant provided by the Department of Mechanical Engineering at Virginia Tech.

References

- [1] Mahmoud I. Hussein, Michael J. Leamy, Massimo Ruzzene, Dynamics of phononic materials and structures: historical origins, recent progress, and future outlook, *Appl. Mech. Rev.* 66 (4) (2014) 040802.
- [2] Wenshan Cai, Vladimir M. Shalaev, *Optical Metamaterials*, vol. 10, Springer, 2010.
- [3] Katia Bertoldi, Vincenzo Vitelli, Johan Christensen, Martin van Hecke, Flexible mechanical metamaterials, *Nat. Rev. Mater.* 2 (11) (2017) 17066.
- [4] Michael M. Sigalas, Eleftherios N. Economou, Elastic and acoustic wave band structure, *J. Sound Vib.* 158 (1992) 377–382.
- [5] M. Sigalas, Eleftherios N. Economou, Band structure of elastic waves in two dimensional systems, *Solid State Commun.* 86 (3) (1993) 141–143.
- [6] Manvir S. Kushwaha, Halevi Peter, Dobrzynski Leonard, Bahram Djafari-Rouhani, Acoustic band structure of periodic elastic composites, *Phys. Rev. Lett.* 71 (13) (1993) 2022.
- [7] Manvir S. Kushwaha, P. Halevi, G. Martinez, Dobrzynski Leonard, Bahram Djafari-Rouhani, Theory of acoustic band structure of periodic elastic composites, *Phys. Rev. B* 49 (4) (1994) 2313.
- [8] J.O. Vasseur, B. Djafari-Rouhani, L. Dobrzynski, M.S. Kushwaha, P. Halevi, Complete acoustic band gaps in periodic fibre reinforced composite materials: the carbon/epoxy composite and some metallic systems, *J. Phys. Condens. Matter* 6 (42) (1994) 8759.
- [9] Manvir S. Kushwaha, Classical band structure of periodic elastic composites, *Int. J. Mod. Phys. B* 10 (9) (1996) 977–1094.
- [10] Zhengyou Liu, Xixiang Zhang, Yiwei Mao, Y.Y. Zhu, Zhiyu Yang, Che Ting Chan, Ping Sheng, Locally resonant sonic materials, *Science* 289 (5485) (2000) 1734–1736.
- [11] Liao Liu, Mahmoud I. Hussein, Wave motion in periodic flexural beams and characterization of the transition between bragg scattering and local resonance, *J. Appl. Mech.* 79 (1) (2012) 011003.
- [12] G.L. Huang, C.T. Sun, Band gaps in a multiresonator acoustic metamaterial, *J. Vib. Acoust.* 132 (3) (2010) 031003.
- [13] R. Zhu, X.N. Liu, G.K. Hu, C.T. Sun, G.L. Huang, A chiral elastic metamaterial beam for broadband vibration suppression, *J. Sound Vib.* 333 (10) (2014) 2759–2773.
- [14] Yuri S. Kivshar, Nikos Flytzanis, Gap solitons in diatomic lattices, *Phys. Rev. A* 46 (12) (1992) 7972.
- [15] Neel Nadkarni, Chiara Daraio, Dennis M. Kochmann, Dynamics of periodic mechanical structures containing bistable elastic elements: from elastic to solitary wave propagation, *Phys. Rev. E* 90 (2) (2014) 023204.
- [16] Bin Liang, Bo Yuan, Jian-chen Cheng, Acoustic diode: rectification of acoustic energy flux in one-dimensional systems, *Phys. Rev. Lett.* 103 (10) (2009) 104301.
- [17] James M. Manimala, C.T. Sun, Numerical investigation of amplitude-dependent dynamic response in acoustic metamaterials with nonlinear oscillators, *J. Acoust. Soc. Am.* 139 (6) (2016) 3365–3372.
- [18] Ali H. Nayfeh, *Introduction to Perturbation Techniques*, John Wiley & Sons, 2011.
- [19] Ali H. Nayfeh, Dean T. Mook, *Nonlinear Oscillations*, John Wiley & Sons, 2008.
- [20] Raj K. Narisetti, Michael J. Leamy, Massimo Ruzzene, A perturbation approach for predicting wave propagation in one-dimensional nonlinear periodic structures, *J. Vib. Acoust.* 132 (3) (2010) 031001.
- [21] Kevin Manktelow, Michael J. Leamy, Massimo Ruzzene, Multiple scales analysis of wave-wave interactions in a cubically nonlinear monoatomic chain, *Nonlinear Dynam.* 63 (12) (2011) 193–203.
- [22] Mohammad H. Abedinnasab, Mahmoud I. Hussein, Wave dispersion under finite deformation, *Wave Motion* 50 (3) (2013) 374–388.
- [23] R. Ganesh, Stefano Gonella, Spectro-spatial wave features as detectors and classifiers of nonlinearity in periodic chains, *Wave Motion* 50 (4) (2013) 821–835.
- [24] W.J. Zhou, X.P. Li, Y.S. Wang, W.Q. Chen, G.L. Huang, Spectro-spatial analysis of wave packet propagation in nonlinear acoustic metamaterials, *J. Sound Vib.* 413 (2018) 250–269.
- [25] M.A. Bukhari, O.R. Barry, Spectro-spatial analyses of a nonlinear metamaterial with multiple nonlinear local resonators., *Nonlinear Dynamics*, 99 (2), 2019–2020, pp. 1539–1560.
- [26] O. Thorp, Massimo Ruzzene, A. Baz, Attenuation and localization of wave propagation in rods with periodic shunted piezoelectric patches, *Smart Mater. Struct.* 10 (5) (2001) 979.
- [27] L. Airoidi, M. Ruzzene, Wave propagation control in beams through periodic multi-branch shunts, *J. Intell. Mater. Syst. Struct.* 22 (14) (2011) 1567–1579.
- [28] Filippo Casadei, Tommaso Delpero, Andrea Bergamini, Paolo Ermanni, Massimo Ruzzene, Piezoelectric resonator arrays for tunable acoustic waveguides and metamaterials, *J. Appl. Phys.* 112 (6) (2012) 064902.
- [29] Andrea Bergamini, Tommaso Delpero, Luca De Simoni, Luigi Di Lillo, Massimo Ruzzene, Paolo Ermanni, Phononic crystal with adaptive connectivity, *Adv. Mater.* 26 (9) (2014) 1343–1347.
- [30] Wanlu Zhou, You Wu, Lei Zuo, Vibration and wave propagation attenuation for metamaterials by periodic piezoelectric arrays with high-order resonant circuit shunts, *Smart Mater. Struct.* 24 (6) (2015) 065021.
- [31] Guobiao Hu, Lihua Tang, Arnab Banerjee, Raj Das, Metastructure with piezoelectric element for simultaneous vibration suppression and energy harvesting, *J. Vib. Acoust.* 139 (1) (2017) 011012.
- [32] Li Shen, Jiu Hui Wu, Siwen Zhang, Zhangyi Liu, Li Jing, Low-frequency vibration energy harvesting using a locally resonant phononic crystal plate with spiral beams, *Mod. Phys. Lett. B* 29 (1) (2015) 1450259.
- [33] Guobiao Hu, Lihua Tang, Raj Das, Metamaterial-inspired piezoelectric system with dual functionalities: energy harvesting and vibration suppression, in: *Active and Passive Smart Structures and Integrated Systems 2017*, ume 10164, International Society for Optics and Photonics, 2017, p. 101641X.
- [34] Guobiao Hu, Lihua Tang, Raj Das, Internally coupled metamaterial beam for simultaneous vibration suppression and low frequency energy harvesting, *J. Appl. Phys.* 123 (5) (2018) 055107.
- [35] Ying Li, Evan Baker, Timothy Reissman, Cheng Sun, Wing Kam Liu, Design of mechanical metamaterials for simultaneous vibration isolation and energy harvesting, *Appl. Phys. Lett.* 111 (25) (2017) 251903.
- [36] S. Tol, F.L. Degertekin, A. Erturk, Gradient-index phononic crystal lens-based enhancement of elastic wave energy harvesting, *Appl. Phys. Lett.* 109 (6) (2016) 063902.
- [37] S. Tol, F.L. Degertekin, A. Erturk, Phononic crystal luneburg lens for omnidirectional elastic wave focusing and energy harvesting, *Appl. Phys. Lett.* 111 (1) (2017) 013503.
- [38] M. Bukhari, O. Barry, On the spectro-spatial wave features in nonlinear metamaterials with multiple local resonators, in: *ASME 2019 International Design Engineering Technical Conferences and Computers and Information in Engineering Conference*, American Society of Mechanical Engineers, 2019.
- [39] Alper Erturk, Daniel J. Inman, *Piezoelectric Energy Harvesting*, John Wiley & Sons, 2011.
- [40] Mahmoud I. Hussein, Michael J. Frazier, Band structure of phononic crystals with general damping, *J. Appl. Phys.* 108 (9) (2010) 093506.